ACS APPLIED MATERIALS & INTERFACES

Research Article

www.acsami.org

Tunable Solar-Heat Shielding Property of Transparent Films Based on Mesoporous Sb-Doped SnO_2 Microspheres

Yusheng Li, Jie Liu, Jie Liang, Xibin Yu,* and Dongjia Li

The Education Ministry Key Laboratory of Resource Chemistry and Shanghai Key Laboratory of Rare Earth Functional Materials, Department of Chemistry, Shanghai Normal University, Shanghai 200234, People's Republic of China

Supporting Information

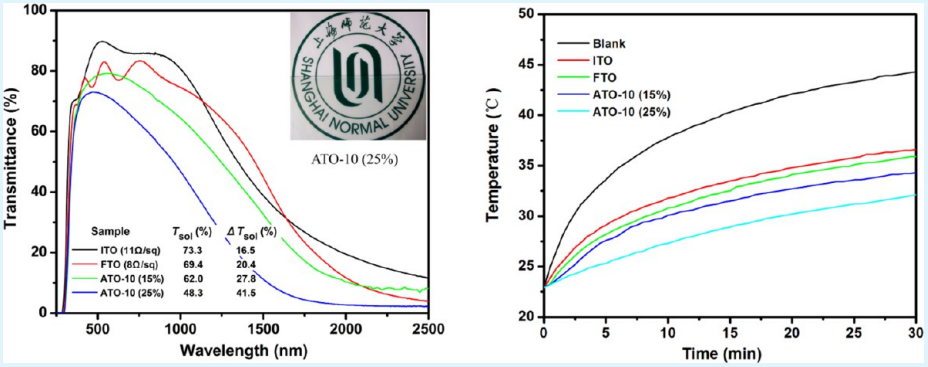

ABSTRACT: In this paper, mesoporous antimony doped tin oxide (ATO) microspheres are synthesized via a solvothermal method from a methanol system with the surfactant followed by a thermal treatment process. Morphology studies reveal that the spherical products obtained by polyvinylpyrrolidone (PVP) templating result in a higher uniformity in size. Such obtained ATO microspheres with a secondary particle size ranging between 200 and 800 nm consist of packed tiny nanocrystals and have high specific surface area (~98 m^2 g^{-1}). The effect of Sb doping on the structural and electrical properties of SnO_2 microspheres is studied. Because of the substitution of Sn^{4+} with Sb^{5+} accompanied by forming a shallow donor level close to the conduction band of SnO_2, a lower resistivity of powder pellet can be achieved, which corresponds to the spectrally selective property of films. The application of ATO microspheres provides an example of transparent coatings; depending on Sb concentration in SnO_2 and solid content of coatings, transparent films with tunable solar-heat shielding property are obtained.

KEYWORDS: *antimony doped tin oxide (ATO), mesoporous microspheres, methanol, solvothermal route, transparent thin films, solar-heat shielding*

INTRODUCTION

Transparent conductive oxides (TCO) play a key role in diverse optoelectronic devices because of their unique combination of high visible light transparency, low transmittance in the near-infrared and electronic conductivity.[1] In recent years, a few researchers have focused on developing different approaches to process TCO films on flat substrates and have achieved significant progress in terms of processing techniques.[2−9] However, most of these approaches are limited to transparent electrode processing, which restricts the use of powder materials for solar-heat shielding. While smart windows are still in their embryonic development stage, glass in architecture has a large promising market for TCO materials. Especially in developing countries, float glasses are often used as construction glasses, which are not used for energy saving.[10]

Historically, TCO materials have been dominated by a family of metal oxides including SnO_2, In_2O_3, ZnO, TiO_2, and CdO, which could be doped with impurities to attain high carrier concentration.[11] A considerable amount of reports are available on the syntheses of Ga-doped ZnO (GZO),[6] Sn-doped In_2O_3 (ITO),[12]Nd-doped TiO_2,[13] Al-doped ZnO (AZO),[14] In-doped ZnO (IZO),[15] and In-doped CdO (ICO)[16] materials. Although reasonable optical properties and electrical conductivities are obtained, few applications with these materials have been reported because of many other problems. For most optoelectronic applications, the indium-based materials are favored. That is because they offer the highest transmissivity for visibility combined with the excellent electrical conductivity. However, indium is not very abundant and is expensive. Therefore, developing some earth abundant and inexpensive alternatives such as ATO is desirable.[17]

As an important alternative of ITO, ATO is of great technological and scientific interest because of its excellent electrical and optical properties. Optimizing the structural properties of ATO is essential to boost its performances. For thin films, the transmittance is strongly dependent on the

Received: December 10, 2014
Accepted: March 16, 2015
Published: March 16, 2015

DOI: 10.1021/am508711p
ACS Appl. Mater. Interfaces 2015, 7, 6574−6583

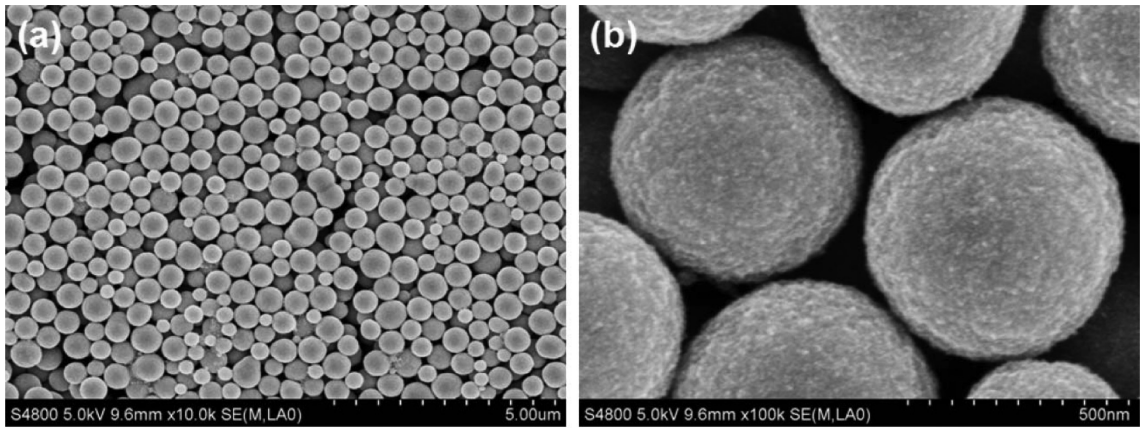

Figure 1. FFSEM images of SnO_2 microspheres synthesized at 180 °C for 6 h in methanol at (a) low and (b) high magnification.

powder dispersibility in coatings. Therefore, to obtain dispersible powder and homogeneous coatings on a large scale, developing solution processes is critical for industrial applications. The mesoporous ATO materials prepared by sol−gel method[18−20] show high surface area and good electrical conductivity, but they are not dispersed easily in the solvents; ATO nanocrystals synthesized by a nonaqueous sol−gel method,[21] which is rather difficult to be scaled up and obtain well-crystalline products without a precise control of various reaction conditions. Usually, such reported approach inevitably results in severe agglomeration of nanoparticles during the thermal treatment, which is needed to incorporate Sb atoms into the SnO_2 lattice. ATO therefore has been synthesized as thin films for some of the aforementioned applications, while the synthesis of well-dispersed mesoporous ATO spheres based films has been relatively unexplored.

Here, we develop a new approach for the preparation of well-dispersed mesoporous ATO microspheres by self-assembly of primary ATO particles using methanol as reaction solvent. The advantage of well-dispersed mesoporous ATO microspheres lies in the resulting mesoporosity and their easy handling. Because microspheres possess a higher packing density than individual particles, which tend to form stable spheres with low-surface energy by agglomerating primary particles.[22,23]

In the research, we find that there are lots of reaction conditions which affect the properties of the products, such as calcination temperature and time, film thickness, solid content, Sb doping concentration. Therefore, we chose one point to start and do the research. We will focus on more details about related reaction conditions in our future work.

In this Research Article, to our knowledge, there is no report of well-dispersed mesoporous ATO microspheres with high surface area formed by individual nanocrystalline obtained by a hydrothermal process which involves the reaction of $SnCl_4$ and $SbCl_3$. In addition, we also find that mesoporous ATO microspheres based film show excellent solar-heat shielding ability as well as high visible transmittance. Furthermore, this approach is also environmentally benign and can be easily industrialized, which is very attractive for energy saving applications.

EXPERIMENTAL SECTION

Synthesis of Mesoporous SnO_2 and ATO Microspheres. All chemicals purchased are used without further purification.

Tin chloride pentahydrate ($SnCl_4·5H_2O$), antimony(III) trichloride ($SbCl_3$), methanol (CH_3OH), ethanol (C_2H_5OH), *n*-propanol, iso-pripanol (C_3H_7OH), KH-570 (97%), polyvinylpyrrolidone (PVP, K30, MW = 50000), Pluronic F127 (MW = 12600) ($EO_{106}PO_{70}EO_{106}$), and Pluronic P123 (MW = 5800) ($EO_{20}PO_{70}EO_{20}$) are acquired from Sigma-Aldrich.

SnO_2 and ATO microspheres are prepared via a solvothermal self-assembly process. In a typical preparation of (0−10 at%) Sb:SnO_2, PVP (0.25 g), $SnCl_4·5H_2O$ (0.175 g) and $SbCl_3$(0−0.0114 g) are mixed in methanol (30 mL). For clarity, the doped proportion of Sb is labeled as ATO-x, where x represents Sb/(Sb + Sn) (mol %). After being mixed and stirred for 10 min, the resulting transparent solution is transferred to a 50 mL Teflon-lined autoclave and heated at 180 °C for 6h, then cooled down naturally. Finally, the resultant precipitate is collected and rinsed with methanol three times to remove impurities, then dried at 60 °C for 12 h. To improve the crystalline quality and other properties of as-prepared ATO-x, the samples are annealed at 500 °C for 2 h in air.

Preparation of Sample Films. The method has been described in previous paper.[24] In detail, to produce a stable suspension, the as-prepared microspheres are ultrasonically treated in deionized water for 30 min. Then, an appropriate amount of WPU (waterborne polyurethanes, 33.3 wt %) and silane coupler KH-570 are added and mixed for 10 min to stabilize the suspension. To fabricate the composite film, the suspension is uniformly cast on the glass slide substrate by doctor-blade method and dried at 60 °C for 1 h. The uniformity of thin film is confirmed by the transmittance in the visible region (T_{vis} > 90%).

Characterization of SnO_2 and ATO Microspheres. XRD analysis is carried out using a Regaku D/max çA X-ray diffractometer (40KV, 30 mA) equipped with Cu Kα radiation (λ = 1.5418 Å). The morphology of the microspheres is characterized by FESEM (S-4800 Hitachi, operated at 5 kV) and TEM (JEOL JEM-2100, operated at 200 kV). The surface area and pore characteristics of the powder material are measured using N_2 physisorption. The N_2 adsorption−desorption isotherms are carried out at 77 K using a Quantachrome NOVA 4000e series surface area analyzer following degassing of the powder samples at 300 °C for 3 h. XPS studies are performed on a Perkine-Elmer PHI 5000C spectrometer with a monochromated Al Kα radiation. The samples are dried in Ar atmosphere before measurements and all the binding energies are corrected with reference to C 1s at 284.6 eV. Resistivity measurements are taken on sample disks (12 mm in diameter) prepared from 0.12 g of powder in an evacuated press under 15 MPa pressure. Resistance across the disk is carried out using Keithley Instruments (Model 2000) in a four-probe mode. The specific resistivity is obtained from the measured resistance R as follows: $\rho = R\pi t/\ln 2$, where t is the disk thickness.

Optical Measurement and Thermal Insulation Application. The optical spectra of the film samples are performed on a Shimadzu UV-3600 UV/vis/NIR Spectrophotometer in the range of 250−2500 nm. To measure thermal insulation properties,[25] the as-fabricated coatings are casted on the precleaned float glass (thickness: 3 mm) of a model house, which is made of 1 cm thick boards. A 2 cm thick board

DOI: 10.1021/am508711p
ACS Appl. Mater. Interfaces 2015, 7, 6574−6583

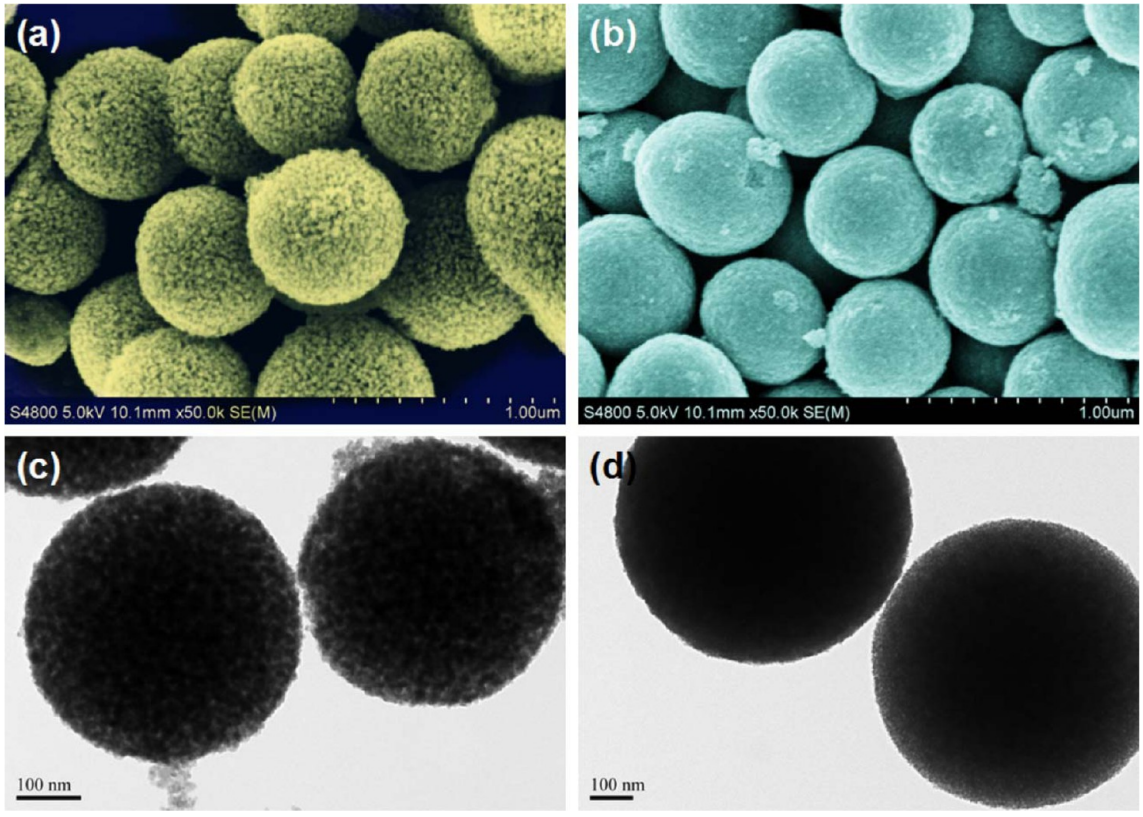

Figure 2. FFSEM and TEM images of (a, c) SnO_2 and (b, d) ATO-10 mesoporous microspheres obtained after calcination at 500 °C for 2 h.

is used to separate the two rooms of the model house. Both rooms have a volume of 6.3×10^3 cm^3 ($15 \times 15 \times 28$ cm^3). Two coated glasses (20×15 cm^2) are installed in the top of the room as two roofs to perform the test with the space sealed during the measurement. The roofs are irradiated by two infrared lamps (Philips, R125 IR R100W), while two digital thermometers are utilized to monitor inner temperature changes of rooms. The whole testing process is carried out in static air at room temperature.

RESULTS AND DISCUSSION

Morphology of Mesoporous SnO_2 and ATO Microspheres. The morphology of the samples is examined with FESEM and TEM. Figure 1a shows a low-magnification FESEM image of the obtained microspheres after the solvothermal reaction at 180 °C for 6 h, which suggests the large-scale formation of well-dispersed microspheres with a diameter of 200−800 nm. As shown in Figure 1b, smooth microspheres with no pores can be seen visually. After further calcination at 500 °C for 2 h in air, while maintaining their self-assembled sphere structure with an urchin-like surface (Figure 2a), it can be clearly observed that the surface of the mesoporous microspheres are formed by aggregating primary SnO_2 particles. These results show that the morphology of product formed before calcination mirrors closely the morphology of calcinated sample and is little influenced by postcalcination treatment.

Interestingly, it is also found that the surface roughness of the microspheres and the average size of nanoparticles decrease a lot with introduction of Sb (10%, at) into SnO_2 microspheres, as shown in Figure 2a and b. More FESEM images about the effect of antimony doping on the morphology of tin oxide are shown in Figure S1 (the Supporting Information).

As reported before, mesopores within microspheres are filled with air which has unique low thermal conductivity, which represents that this mesoporous structure is more likely to reduce heat flow and retain excellent thermal insulation and thermal preservation performance.[26] For the desired purpose of a heat insulation material, such a nanoscale structure is preferred as it can help to improve the solar heat block properties of ATO thin films. The interesting nanostructure of mesoporous microspheres composed of tiny packed nanocrystallites is further confirmed by TEM. High-magnification TEM images (Figure 2c and d) show the isolated SnO_2 (Figure 2c) and ATO (Figure 2d) mesoporous microspheres at same magnification.

Influence of the Reaction Parameters on the Morphology of the Products. To investigate the critical factors in solvothermal process that lead to the formation of well-dispersed mesoporous products of SnO_2 and ATO nanoparticle aggregates, a series of experiments are conducted. As seen in Figure S2 (Supporting Information), the FESEM micrographs depict the morphology of SnO_2 obtained in the reaction solvent without surfactants. It is obvious that nonuniform and smooth microspheres are obtained in methanol system. When other alcohols (e.g., isopropano, ethanol, propanol) are used to substitute methanol, rough peanut-like particles, particles with reticular structure and irregular aggregates of small nanoparticles are observed. Then, based on the methanol system, we have tried to adjust the uniformity of the spheres by adding soft template (PVP, F123, P127). As we can see from Figure S3 (Supporting Information), large-scale, uniform spheres are obtained with addition of PVP, while F127 hindered the nanoparticles from assembling into spheres. For P123, the spheres are still

DOI: 10.1021/am508711p
ACS Appl. Mater. Interfaces 2015, 7, 6574−6583

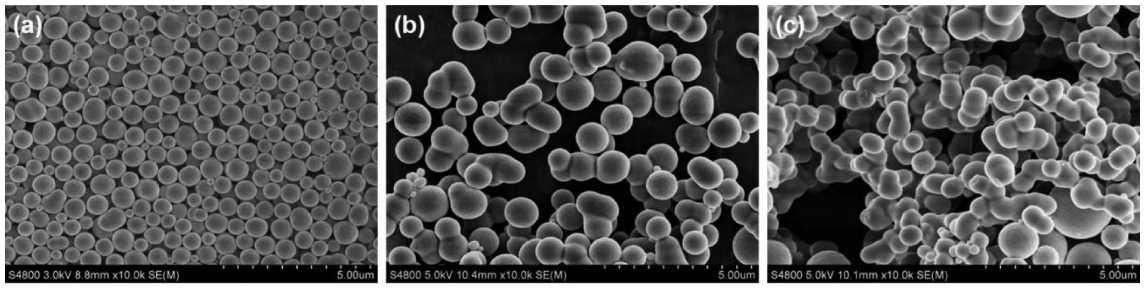

Figure 3. FESEM images of the ATO-10 solvothermally prepared under a concentration of (a) 17, (b) 34, and (c) 68 mM at 180 °C for 6 h in methanol.

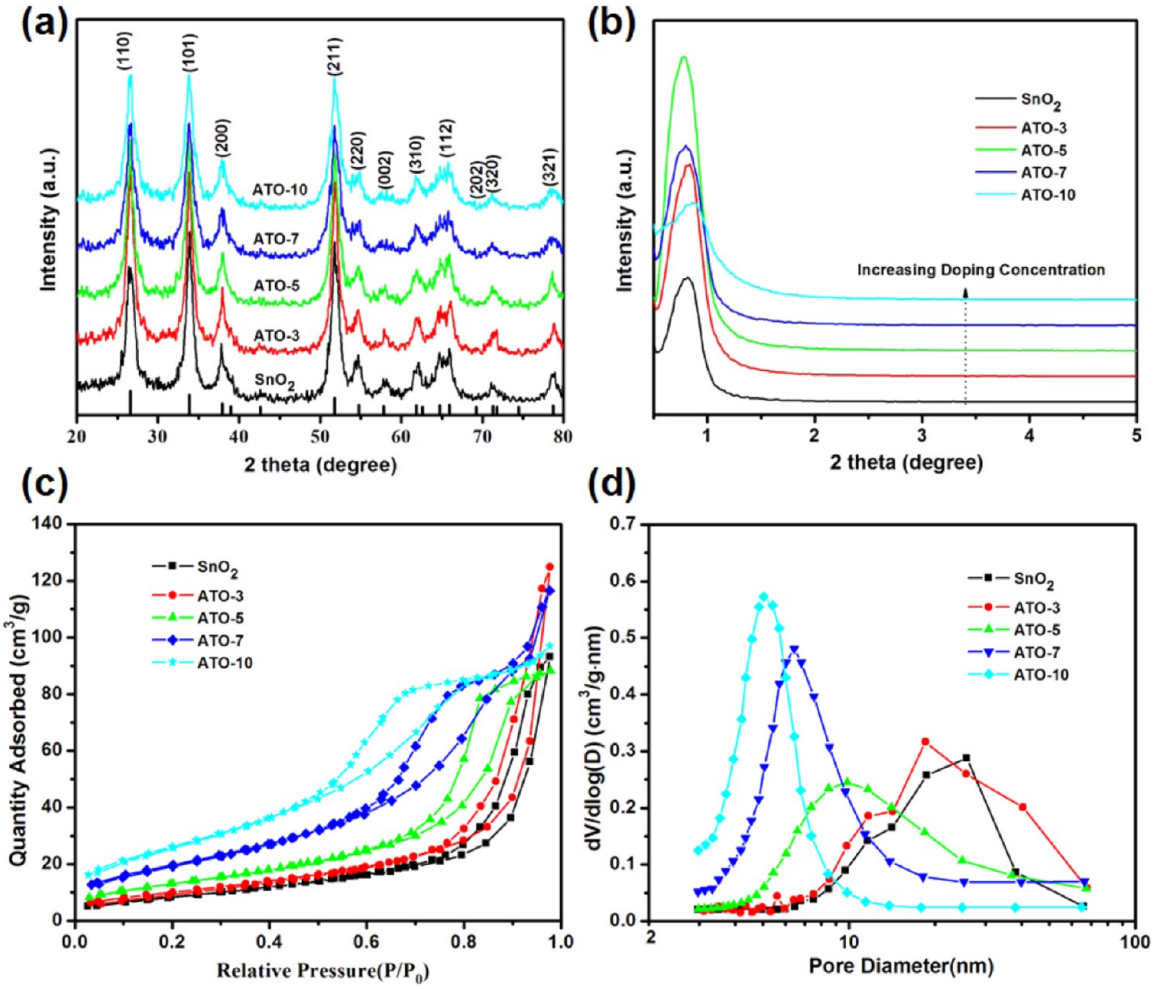

Figure 4. (a) Wide-angle XRD patterns, (b) low-angle XRD patterns, (c) N_2 adsorption−desorption isotherm, and (d) pore size distribution of the as synthesized ATO microspheres with varying Sb content thermally treated at 500 °C for 2 h.

nonuniform. The results demonstrate that methanol plays a key role in forming microspheres and PVP could help tune the size of spheres in the methanol system.

The following experiments are taken to investigate the influence of precursor concentration on the morphology of samples synthesized in the methanol system. For this purpose, samples are prepared with PVP and with addition of $SbCl_3$ (10%, atm) at 17, 34, and 68 mM $SnCl_4{\cdot}5H_2O$. As the Sn concentration increased to 34−68 mM, spheres join together and form irregular structure and bigger spheres. Compared to the regular microspheres obtained at 17 mM (Figure 3a), the ATO samples synthesized at 34 mM, the microspheres are found to retain most of their dispersity characteristics and morphology except that the diameters increase to 1−2 μm (Figure 3b). When Sn concentration further increases to 68 mM (Figure 3c), severe agglomeration occurs. The driving force behind agglomeration of nanostructure is the overall surface energy reduction of the system. Therefore, as the process is usually irreversible, it is necessary to reduce agglomeration. Also, it is important to note that microspheres obtained under low Sn concentration system are preferable since the obtained microspheres have high porosity as well as small diameter.

DOI: 10.1021/am508711p
ACS Appl. Mater. Interfaces 2015, 7, 6574−6583

Influence of Sb Concentration on Structure. To verify the crystallization of the ATO microspheres and to track the nanocrystal growth, we conduct Sb concentration-dependent XRD measurements. Figure 4a shows wide-angle XRD patterns of the thermal treated samples. Crystalline materials are achieved under all conditions, with only tetragonal rutile SnO_2 (JCPDS Card No. 41-1445) diffraction peaks detected, and no other impurity phases in XRD peaks are found. What is noteworthy is that a slight variation in broadening and relative intensity can be seen.

As shown in Table 1, the amount of Sb in calcinated ATO microspheres is measured by inductively coupled plasma (ICP),

Table 1. Amount of Sb in Calcinated ATO Microspheres Prepared at Different Sb Precursor Concentrations

$SbCl_3$ precursor (atom %)	0	3	5	7	10
Sb in ATO microspheres (atom %)	0	2.81	4.75	6.56	9.32

which proves a success in doping of Sb in SnO_2. Owing to the introduction of dopant ions in the reaction system, these influences are distributed to variations in nanocrystal size. In detail, as seen from Table S1 (Supporting Information), a steady decrease in the particle size along with the presence of Sb ions is observed for the peaks corresponding to the (110), (101), (211) diffraction. Accordingly, the increasing Sb concentration results in the decrease in crystallite size estimated from Scherrer's formula from 12.2 nm for SnO_2 to 10.3, 8.9, 8.0, and 6.6 nm for SnO_2 nanoparticles doped with 3, 5, 7, 10, respectively. In some degree, the particle size decreases steadily with increasing Sb concentration shares the same mechanism with Sb-VO_2 system,[27] but there is no phase transition in Sb-SnO_2. In this system, it is noteworthy that the substitution of Sn^{4+} (69 pm in six-coordination) with Sb^{5+} (60 pm in six-coordination), a slightly smaller ion, along with a little amount of bigger Sb^{3+} (76 pm in six-coordination), should shift the diffraction peaks to higher angles, due to the decrease in crystal cell size. Interstitial Sb^{3+}/Sb^{5+} ions (mainly Sb^{5+}) might increase crystalline cell volume as well, even their presence is energetically unenjoyable. Therefore, it is probable that a combination of these contributions leads to the negligible shift. As shown in Figure 4b, the intensities of the low-angle XRD peaks first increase and then decrease as the amount of Sb increases. This indicates that the present meso-SnO_2 materials slightly increase the regularity of their mesostructures upon the addition of antimony to 5%. However, with the concentration of antimony in SnO_2 increasing to 10%, the regularity of the samples' mesostructures decreases a little.

Since the microspheres consist of numberous nanoparticles, a high surface area can be expected, which is confirmed by nitrogen adsorption tests. The N_2 adsorption−desorption isotherm is identified as type IV isotherm in the relative pressure range (P/P_0) of 0.8−1.0, as shown in Figure 4c, which shows a hysteresis loop characteristic to the meso-ATO microspheres with Sb doping content of 0%, 3%, 5%, 7%, 10%, respectively. According to the BET (Brunauer−Emmett−Teller) method, the surface area of the samples gradually decreases from 98, 73, 48, 38 $m^2\ g^{-1}$ (10%, 7%, 5%, 3% Sb, respectively) to 31 $m^2\ g^{-1}$ for SnO_2. This surface area (98 $m^2\ g^{-1}$) is considerably higher than those of the reported mesoporous ATO spheres with similar doping concentration.[28] This is attributed to the fact that microspheres have a higher packing density and stable physical structure than individual nanoparticles. The existence of mesopores in the ATO microspheres is confirmed by hysteresis loops. The porosity corresponds to the interstitial pores formed between nanoparticles upon agglomeration. With increasing Sb content, the hysteresis loops shift to lower pressures, which indicates pore size reduction. For the samples obtained at 500 °C, broad, but distinguished BJH pore distribution curves can be seen from Figure 4d. As shown in Table 2, the average size of pores decreases from 18.66 to 5.69 nm with increasing Sb contents in the series.

Table 2. Summary of ATO Pore Characteristics with Varying Sb Content

sample	BET surface area ($m^2\ g^{-1}$)	pore volume ($cm^3\ g^{-1}$)	average pore size (nm)
SnO_2	31.92	0.146	18.66
ATO-3	38.29	0.197	18.49
ATO-5	48.49	0.140	11.64
ATO-7	73.47	0.185	5.70
ATO-10	98.00	0.150	5.69

Influence of Sb Concentration on Electrical Conductivity. Resistivity measurements are performed on pellets prepared from as-synthesized powder materials to investigate the interplay between doping concentration and electrical conductivity (Figure 5). The graph exhibits an apparent change

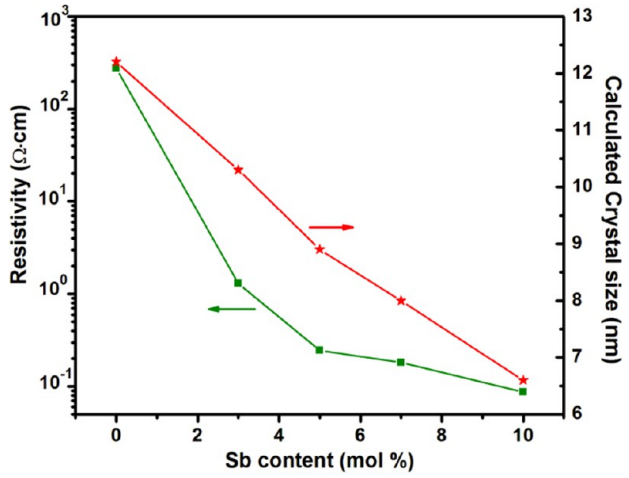

Figure 5. Variation of resistivity, determined by a four-point probe, and crystal size, calculated using Debye−Scherrer formula, of ATO.

in resistivity with Sb contents, which can be ascribed to the increase in free charge carrier concentration via the formation of oxygen vacancies.[29−31] It can be observed that the electrical resistivity and nanoparticles size of ATO powders shows a significant decrease just only by adding a really small amount of antimony. In addition to the influence of applied pressure on the preparation of pellet, increasing the interfacial area and reducing the porosity between ATO nanoparticles by antimony doping should lead to a lower resistivity, which contributes to more charge transport pathways.

Even though the resistivity change is not linear, it follows a trend often observed for ATO.[32,33] Although the resistivities of the doped samples ($1.3−8.68 \times 10^{-2}$ Ω·cm) are higher than the obtained for dense films (down to 1×10^{-3} Ω·cm), the values are still lower than the resistivity previously reported for ATO

DOI: 10.1021/am508711p
ACS Appl. Mater. Interfaces 2015, 7, 6574−6583

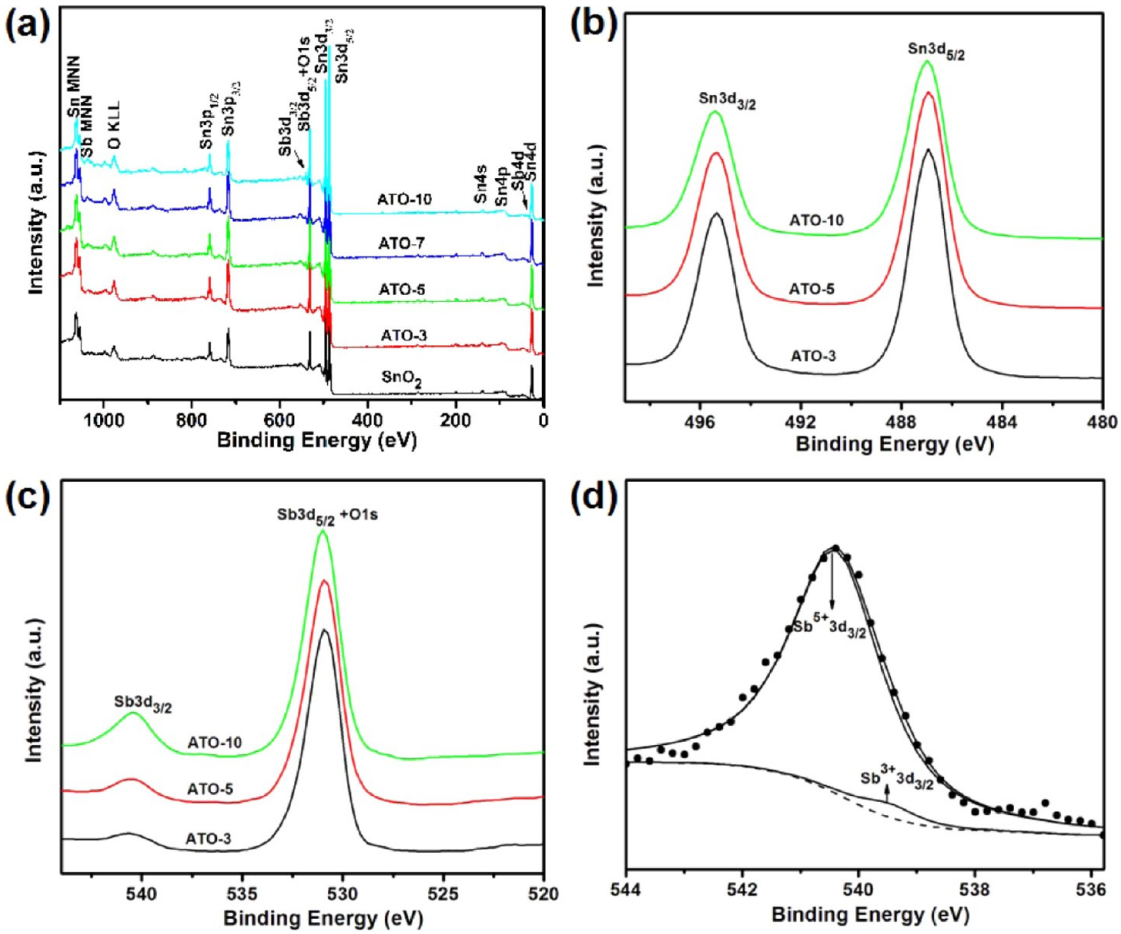

Figure 6. Sn and Sb composition of all samples were determined by XPS with representative data from ATO powders with different doping levels. (a) survey spectra (b) high-resolution XPS spectra for Sn 3d (c) high-resolution XPS spectra for Sb 3d and O 1s (d) spectrum of the Sb $3d_{3/2}$ peak for ATO-10 sample and corresponding fit data. All the prepared materials had been calcined at 500 °C for 2 h in air.

nanorods (0.8 Ω·cm) and mesoporous ATO material (0.14 Ω·cm).[20,34]

While Sb^{5+} ions act as electron donors, forming a shallow donor level close to the conduction band of SnO_2, Sb^{3+} ions behave as an electron acceptor. If Sb^{5+} and Sb^{3+}coexist, which is often observed for ATO products, the resistivity is given by the ratio of Sb^{5+} and Sb^{3+}, which is carried out by XPS.

Quantitative compositional information can be given by comparing the Sn 3d peaks and Sb 3d peaks, the possible convolution of antimony oxide state. Evidence of Sb n-doping is provided via four-point probe measurement. Figure 6 shows the high-resolution XPS spectra of Sn 3d and Sb 3d. The survey XPS spectra (Figure 6a) clearly indicate that existence of Sn, Sb and O elements in the ATO microspheres. As shown in Figure 6b, the binding energies of Sn $3d_{5/2}$ and Sn $3d_{3/2}$ for ATO are located at 487.1 and 495.5 eV, respectively, typically assigned to the presence of Sn^{4+}. The binding energy of the Sb 3d is reported to be in the range of 537−543 eV (Figure 6c). The Sb 3d peak is split into two peaks at 540.44 and 539.51 eV corresponding to Sb^{3+} $3d_{3/2}$ and Sb^{5+} $3d_{3/2}$, respectively. The deconvolution (Figure 6d) illustrates that most of the Sb ions are at the Sb (V) oxidition state with a small amount of Sb (III), which is consistent with the n-type doped semiconductor behavior of ATO in the literature.[7] Therefore, these results confirm that the decrease of primary particle size and resistivity are caused by Sb^{5+} with increasing doping levels.

Influence of Sb Concentration and Film Thickness on Optical Properties. It is universally accepted that substitution of tetravalent tin cations by pentavalent antimony cations in the SnO_2 crystal lattice endows generation of free carriers, resulting in the ATO with low resistivity compared with pure counterparts.[35−38] Under the optimized reaction conditions, we have investigated the optical properties of as-prepared films from ATO coatings (at a solid fixed content of 15%). UV−vis-NIR optical spectra (Figure 7a and 7b) of the ATO films indicate the generation of free charge carriers upon dopant incorporation. As is shown in Figure 7a, all the doped films exhibit broad absorption in the red visible region and their absorption strength reaches a maximum in the NIR region. In addition, the absorption peak shifts to higher energies and increases in intensity with the increasing doping content. These spectral characteristics are consistent with TCO materials which exhibit localized surface plasmon resonance absorption.[11,39−41] Notably, all the doped films show high visible-light transparency and poor transmittance in the NIR, which propose that the potential use of ATO for spectrally selective coatings (Figure 7b), while there is not big change of reflective index with the change of antimony content of ATO (Figure S4, Supporting Information). Moreover, the transmittance spectra of multilayer films of 5% doped ATO thin films are showed in Figure S5 (Supporting Information), which indicate that the transparency in the visible and NIR spectrum is decreased with increasing the thickness of films.

DOI: 10.1021/am508711p
ACS Appl. Mater. Interfaces 2015, 7, 6574−6583

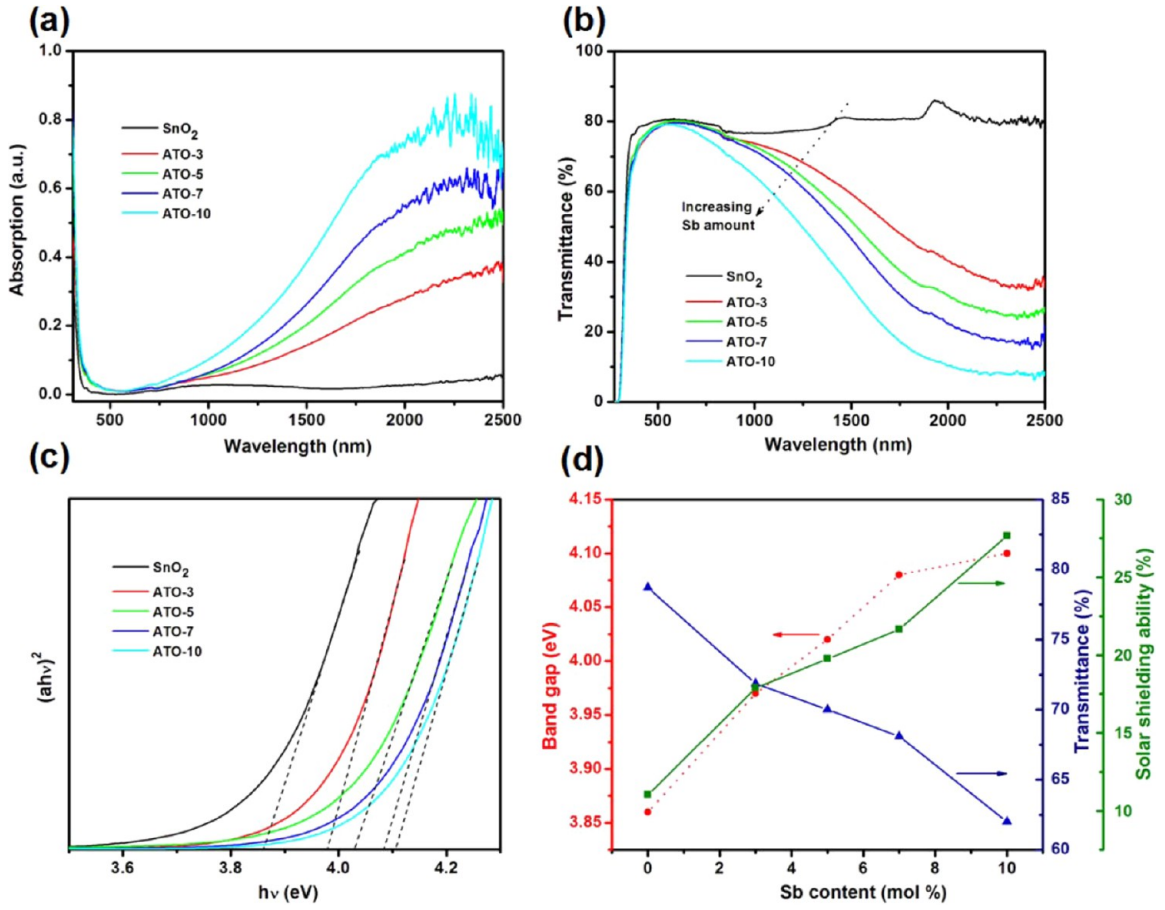

Figure 7. Influence of Sb content on the optical properties of ATO microspheres. (a) Optical absorption spectra of ATO films as a function of Sb doping. (b) Optical transmission spectra of ATO films at different nominal Sb amounts. (c) Tauc plots of the $(\alpha h\nu)^2$ versus $h\nu$ curves of ATO films with different antimony content. The optical band gap for each of them has been derived from the extrapolation to $\alpha = 0$. (d) The value of band gap and integrated optical properties of ATO samples.

The optical band gaps are calculated using Tauc plots (shown in Figure 7c). Compared with the band gap of the bulk SnO_2 (3.62 eV), the band gap increase of SnO_2 nanoparticles in microspheres (3.86 eV) is attributed to quantum confinement-induced band gap increase.[42−44] Corresponding to the transmission spectrum, Tauc plots of the as-prepared films exhibit a shift to higher band gap (3.86−4.10 eV) with increasing dopant concentration. In addition to the quantum confinement effect upon Sb doping, this blue shift can be interpreted as result of Burstein−Moss effect where the carrier concentration increase leads to an upward shift to the Fermi level within the conduction band.[33]

For all the films, the integrated solar transmittance (T_{sol}, 250−2500 nm), visible transmittance (T_{vis}, 380−780 nm), and NIR transmittance (T_{NIR}, 780−2500 nm) are obtained from the measured spectra using the following equation:

$$T_i = \frac{\int_{\lambda 1}^{\lambda 2} E\lambda T\lambda \, d\lambda}{\int_{\lambda 1}^{\lambda 2} E\lambda \, d\lambda}$$

Where the i denotes vis, NIR, or sol, T_λ denotes the transmittance at wavelength λ (nm), and E_λ (W m^{-2} nm^{-1}) is the power of solar irradiance spectrum (AM 1.5).

As shown in Figure 7d, the values of T_{sol} (250−2500 nm) (where a lower T_{sol} illustrates a better solar shielding property) decrease with increasing Sb concentration, while the solar shielding ability (ΔT_{sol}, a difference of T_{sol} between blank glass and the sample) and the band gap increase steadily. More details about values of T_i and ΔT_{sol} are shown in Table S2 (Supporting Information).

Solar Shielding Capability of Mesoporous ATO Microsphere-Based Films. The TCO glasses are well-known and widely harnessed as effective infrared rejection material.[45−47] As shown in Figure 8, ITO and FTO show high transparency in visible light, but the ΔT_{sol} are not strong as ATO-10 (solid content of 15%, 25%). The value of ΔT_{sol} increases as the ATO-10 content increased. When the application comes to solar film of buildings and cars, depending on the needs (e.g., windows of house building need good day-lighting, while low visible transparency is indeed preferable for private space of the car), different visible transparency and solar shielding ability could be provided. Compared with the reported ATO films prepared from spin-coating (T_{sol}, 58.56%)[48] and sol−gel methods,[4] the ATO-10 (25%) film (T_{sol}, 48.3%) shows better solar heat reduction.

To test the solar shielding ability of ATO mesoporous microspheres as fillers for transparent composite, a simulated experiment is conducted by irradiating two sealed building models (Figure 9a) covered by blank glass and film sample. Then, the temperature is measured under irradiation. Although the increment of temperature could be depressed by the substitution of blank glass with commercial FTO or ITO glass, prolonged irradiation still cause the temperature to increase

DOI: 10.1021/am508711p
ACS Appl. Mater. Interfaces 2015, 7, 6574−6583

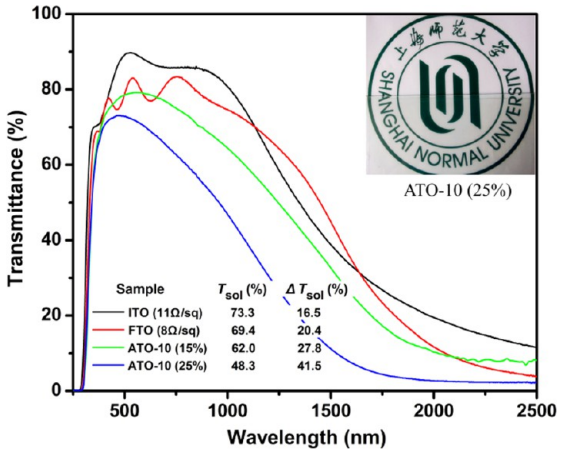

Figure 8. Transmittance spectra and computerized optical properties of ITO, FTO, and ATO-10 films. Inset is the film sample based on ATO-10 suspension (solid content 25%).

remarkably due to its incompleteness of wavelength below 1250 nm. In contrast, excellent solar shielding ability is realized by adopting ATO-10 (solid content of 15%, 25%) film. As we can see from Figure 9b, after being irradiated by infrared lamps for 30 min, the inner temperature of ATO-10 film shows further 1.5−4.5 °C temperature depression compared to those of ITO and FTO glasses. The results are consistent with the values of ΔT_{sol} shown in Figure 8.

CONCLUSIONS

In conclusion, the successful synthesis of well-dispersed mesoporous ATO microspheres consisting of nanocrystals via a solvothermal route in methanol and PVP system is presented. The specific surface area and pore size of the as-obtained ATO microspheres could be deliberately controlled by varying the concentration of $SbCl_3$. The as-synthesized ATO nanoparticles in the microspheres show a high electrical conductivity. Furthermore, the optical properties provide strong evidence that the Sb occupies substitutional sites, effectively creating free electrons in the nanoparticles. Therefore, the high specific area microstructure and spectrally selective optical properties of the as-prepared ATO microspheres make them valuable alternatives to much more rare and expensive ITO. Uniform and transparent films synthesized directly from a water based dispersion of mesoporous ATO microsperes, which effectively reduce the NIR transparency, open up a way to potential use in smart windows.

ASSOCIATED CONTENT

Supporting Information

FESEM images about the reaction parameters on the morphology of the products, crystallite size calculated from Scherrer formula for the prepared mesoporous microspheres according to Sb amount, reflectance spectra of mesoporous SnO_2 and ATO microspheres based films, transmission spectra of single- and multilayer 5% doped ATO films, and solar energy control properties of sample films with different Sb content (at a fixed solid content of 15%). This material is available free of charge via the Internet at http://pubs.acs.org.

AUTHOR INFORMATION

Corresponding Author

*Email: xibinyu@shnu.edu.cn; Tel: +86-21-64324528.

Notes

The authors declare no competing financial interest.

ACKNOWLEDGMENTS

This study is supported by the first-class discipline construction plan in Shanghai University, PCSIRT (IRT1269), Shanghai Science & Technology Committee (12521102501), Shanghai Educational Committee (11ZR1426500, 14ZZ127), and Program of Shanghai Normal University (DZL124).

REFERENCES

(1) Pasquarelli, R. M.; Ginley, D. S.; Hayre, R. O. Solution Processing of Transparent Conductors: from Flask to Film. *Chem. Soc. Rev.* **2011**, *40*, 5406−5441.

(2) Müller, V.; Rasp, M.; Rathouský, J.; Schütz, B.; Niederberger, M.; Fattakhova-Rohlfing, D. Transparent Conducting Films of Antimony-Doped Tin Oxide with Uniform Mesostructure Assembled from Preformed Nanocrystals. *Small* **2010**, *6*, 633−637.

(3) Lee, J. H.; Lee, S.; Li, G. L.; Petruska, M. A.; Paine, D. C.; Sun, S. H. A Facile Solution-Phase Approach to Transparent and Conducting ITO Nanocrystal Assemblies. *J. Am. Chem. Soc.* **2012**, *134*, 13410−13414.

(4) Koebel, M. M.; Nadargi, D. Y.; Jimenez-Cadena, G.; Romanyuk, Y. E. Transparent, Conducting ATO Thin Films by Epoxide-Initiated

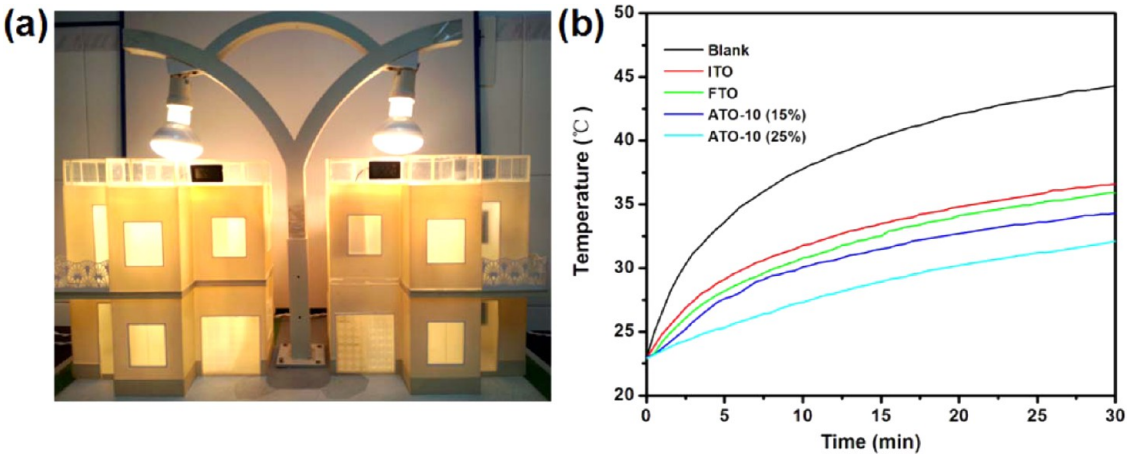

Figure 9. (a) Building models of the testing system. (b) Dependence of temperature on irradiation time for blank glass, commercial ITO, and FTO glasses, and ATO-10 films (solid content of 15%, 25%).

DOI: 10.1021/am508711p
ACS Appl. Mater. Interfaces 2015, 7, 6574−6583

Sol−Gel Chemistry: A Highly Versatile Route to Mixed-Metal Oxide Films. *ACS Appl. Mater. Interfaces* **2012**, *4*, 2464−2473.
(5) Luo, L.; Rossell, M. D.; Xie, D.; Erni, R.; Niederberger, M. Microwave-Assisted Nonaqueous Sol−Gel Synthesis: From Al: ZnO Nanoparticles to Transparent Conducting Films. *ACS Sustainable Chem. Eng.* **2013**, *1*, 152−160.
(6) Gaspera, E. D.; Bersani, M.; Cittadini, M.; Guglielmi, M.; Pagani, D.; Noriega, R.; Mehra, S.; Salleo, A.; Martucci, A. Low-Temperature Processed Ga-Doped ZnO Coatings from Colloidal Inks. *J. Am. Chem. Soc.* **2013**, *135*, 3439−3448.
(7) Sharma, S.; Volosin, A. M.; Schmitt, D.; Seo, D. K. Preparation and Electrochemical Properties of Nanoporous Transparent Antimony-Doped Tin Oxide (ATO) Coatings. *J. Mater. Chem. A* **2013**, *1*, 699−706.
(8) Chen, Z. X.; Li, W. C.; Li, R.; Zhang, Y. F.; Xu, G. Q.; Cheng, H. S. Fabrication of Highly Transparent and Conductive Indium-Tin Oxide Thin Films with a High Figure of Merit via Solution Processing. *Langmuir* **2013**, *29*, 13836−13842.
(9) Wang, Y. D.; Brezesinski, T.; Antonietti, M.; Smarsly, B. Ordered Mesoporous Sb-, Nb-, and Ta-Doped SnO_2 Thin Films with Adjustable Doping Levels and High Electrical Conductivity. *ACS Nano* **2009**, *3*, 1373−1378.
(10) Gao, Y. F.; Wang, S.; Kang, L.; Chen, Z.; Du, J.; Liu, X.; Luo, H.; Kanehira, M. VO_2-Sb:SnO_2 Composite Thermochromic Smart Glass Foil. *Energy Environ. Sci.* **2012**, *5*, 8234−8237.
(11) Comin, A.; Manna, L. New Materials for Tunable Plasmonic Colloidal Nanocrystals. *Chem. Soc. Rev.* **2014**, *43*, 3957−3975.
(12) Garcia, G.; Buonsanti, R.; Runnerstrom, E. L.; Mendelsberg, R. J.; Llordes, A.; Anders, A.; Richardson, T. J.; Milliron, D. J. Dynamically Modulating the Surface Plasmon Resonance of Doped Semiconductor Nanocrystals. *Nano Lett.* **2011**, *11*, 4415−4420.
(13) Trizio, L. D.; Buonsanti, R.; Schimpf, A. M.; Llordes, A.; Gamelin, D. R.; Simonutti, R.; Milliron, D. J. Nb-Doped Colloidal TiO_2 Nanocrystals with Tunable Infrared Absorption. *Chem. Mater.* **2013**, *25*, 3383−3390.
(14) Buonsanti, R.; Llordes, A.; Aloni, S.; Helms, B. A.; Million, D. J. Tunable Infrared Absorption and Visible Transparency of Colloidal Aluminum-Doped Zinc Oxide Nanocrystals. *Nano Lett.* **2011**, *11*, 4706−4710.
(15) Liang, X. Y.; Ren, Y. P.; Bai, S.; Zhang, N.; Dai, X. L.; Wang, X.; He, H. P.; Jin, C. H.; Ye, Z. Z.; Chen, Q.; Chen, L. W.; Wang, J. P.; Jin, Y. Z. Colloidal Indium-Doped Zinc Oxide Nanocrystals with Tunable Work Function: Rational Synthesis and Optoelectronic Applications. *Chem. Mater.* **2014**, *26*, 5169−5178.
(16) Gordon, T. R.; Paik, T.; Klein, D. R.; Naik, G. V.; Caglayan, H.; Boltasseva, A.; Murray, C. B. Shape-Dependent Plasmonic Response and Directed Self-Assembly in A New Semiconductor Building Block, Indium-Doped Cadmium Oxide (ICO). *Nano Lett.* **2013**, *13*, 2857−2863.
(17) Shigesato, Y. In Based TCOs. In *Handbook of Transparent Conductors*; Ginley, D. S., Hosono, H., Paine, D. C., Eds.; Springer Science+Business Media: New York, 2010; pp 149−169.
(18) Wang, Y. D.; Djerdj, I.; Smarsly, B. Antimony-Doped SnO_2 Nanopowders with High Crystallinity for Lithium-Ion Battery Electrode. *Chem. Mater.* **2009**, *21*, 3202−3209.
(19) Rolison, D. R.; Dunn, B. Electrically Conductive Oxide Aerogels: New Materials in Electrochemistry. *J. Mater. Chem.* **2001**, *11*, 963−980.
(20) Volosin, A. M.; Sharma, S.; Traverse, C.; Newmanb, N.; Seo, D. K. One-Pot Synthesis of Highly Mesoporous Antimony-Doped Tin Oxide from Interpenetrating Inorganic/Organic Networks. *J. Mater. Chem.* **2011**, *21*, 13232−13240.
(21) Conti, T. G.; Chiquito, A. J.; da Silva, R. O.; Longo, E.; Leite, E. R. Electrical Properties of Highly Conducting SnO_2:Sb Nanocrystals Synthesized using a Nonaqueous Sol−Gel Method. *J. Am. Ceram. Soc.* **2010**, *93*, 3862−3866.
(22) Chen, D. H.; Caruso, R. A. Recent Progress in the Synthesis of Spherical Titania Nanostructures and Their Applications. *Adv. Funct. Mater.* **2013**, *23*, 1356−1374.
(23) Demir-Cakan, R.; Hu, Y. S.; Antonietti, M.; Maier, J.; Titirici, M. M. Facile One-Pot Synthesis of Mesoporous SnO_2 Microspheres via Nanoparticles Assembly and Lithium Storage Properties. *Chem. Mater.* **2008**, *20*, 1227−1229.
(24) Gao, Y. F.; Wang, S. B.; Luo, H. J.; Dai, L.; Cao, C. X.; Liu, Y. L.; Chen, Z.; Kanehira, M. Enhanced Chemical Stability of VO_2 Nanoparticles by the Formation of SiO_2/VO_2 Core/Shell Structures and the Application to Transparent and Flexible VO_2-Based Composite Foils with Excellent Thermochromic Properties for Solar Heat Control. *Energy Environ. Sci.* **2012**, *5*, 6104−6110.
(25) Guo, C. S.; Yin, S.; Huang, Y. F.; Dong, Q.; Sato, T. Synthesis of $W_{18}O_{49}$ Nanorod via Ammonium Tungsten Oxide and Its Interesting Optical Properties. *Langmuir* **2011**, *27*, 12172−12178.
(26) Wang, M.; Zeng, Q. Q.; Zhao, B.; He, D. N. Application of Tailored Silica Microspheres in Coatings: Synthesis, Characterization, Thermal and Hydrophobic Properties. *J. Mater. Chem. A* **2013**, *1*, 11465−11472.
(27) Gao, Y. F.; Cao, C. X.; Dai, L.; Luo, H. J.; Kanehira, M.; Ding, Y.; Wang, Z. L. Phase- and Shape-Controlled VO_2 nanostructures by antimony doping. *Energy Environ. Sci.* **2012**, *5*, 8708−8715.
(28) Wang, Y. D.; Chen, T. Nonaqueous and Template-Free Synthesis of Sb Doped SnO_2 Microspheres and Their Application to Lithium-Ion Battery Anode. *Electrochim. Acta* **2009**, *54*, 3510.
(29) NTz, T.; Haase, M. Wet-Chemical Synthesis of Doped Nanoparticles: Optical Properties of Oxygen-Deficient and Antimony-Doped Colloidal SnO_2. *J. Phys. Chem. B* **2000**, *104*, 8430−8437.
(30) Chen, F.; Li, N.; Shen, Q.; Wang, C. B.; Zhang, L. M. Fabrication of Transparent Conducting ATO Films Using the ATO Sintered Targets by Pulsed Laser Deposition. *Sol. Energy Mater. Sol. Cells* **2012**, *105*, 153−158.
(31) Park, G. C.; Hwang, S. M.; Lim, J. H.; Joo, J. Growth Behavior and Electrical Performance of Ga-Doped ZnO Nanorod/p-Si Heterojunction Diodes Prepared Using A Hydrothermal Method. *Nanoscale* **2014**, *6*, 1840−1847.
(32) Wang, L. S.; Lu, H. F.; Hong, R. Y.; Feng, W. G. Synthesis and Electrical Resistivity Analysis of ATO-Coated Talc. *Powder Technol.* **2012**, *224*, 124−128.
(33) Mazloom, J.; Ghodsi, F. E.; Gholami, M. Fiber-like Stripe ATO (SnO_2: Sb) Nanostructured Thin Films Grown by Sol−Gel Method: Optical, Topographical, and Electrical Properties. *J. Alloys Compd.* **2013**, *579*, 384−393.
(34) Lu, H. F.; Hong, R. Y.; Wang, L. S.; Xie, H. D.; Zhao, S. Q. Preparation of ATO Nanorods and Electrical Resistivity Analysis. *Mater. Lett.* **2012**, *68*, 237−239.
(35) Li, Z. Q.; Yin, Y. L.; Liu, X. D.; Li, L. Y.; Liu, H.; Song, Q. G. Electronic Structure and Optical Properties of Sb-Doped SnO_2. *J. Appl. Phys.* **2009**, *106*, 083701−083705.
(36) Thangaraju, B. Structural and Electrical Studies on Highly Conducting Spray Deposited Fluorine and Antimony Doped SnO_2 Thin Films from $SnCl_2$ Precursor. *Thin Solid Films* **2002**, *402*, 71−78.
(37) Saadeddin, I.; Hilal, H. S.; Pecquenard, B.; Marcus, J.; Mansouri, A.; Labrugerea, C.; Subramanian, M. A.; Campet, G. Simultaneous Doping of Zn and Sb in SnO_2 Ceramics: Enhancement of Electrical Conductivity. *Solid State Sci.* **2006**, *8*, 7−13.
(38) Saadeddin, I.; Pecquenard, B.; Manaud, J. P.; Decourt, R.; Labrugerea, C.; Buffeteau, T.; Campet, G. Synthesis and Characterization of Single and Co-Doped SnO_2 Thin Films for Optoelectronic Applications. *Appl. Surf. Sci.* **2007**, *253*, 5240−5249.
(39) Kanehara, M.; Koike, H.; Yoshinaga, T.; Teranishi, T. Indium Tin Oxide Nanoparticles with Compositionally Tunable Surface Plasmon Resonance Frequencies in the Near-IR Region. *J. Am. Chem. Soc.* **2009**, *131*, 17736−177367.
(40) Mendelsberg, R. J.; Garcia, G.; Li, H. B.; Manna, L.; Milliron, D. J. Understanding the Plasmon Resonance in Ensembles of Degenerately Doped Semiconductor Nanocrystals. *J. Phys. Chem. C* **2012**, *116*, 12226−12231.
(41) Liu, X.; Swihart, M. T. Heavily-Doped Colloidal Semiconductor and Metal Oxide Nanocrystals: An Emerging New Class of Plasmonic Nanomaterials. *Chem. Soc. Rev.* **2014**, *43*, 3908−3920.

DOI: 10.1021/am508711p
ACS Appl. Mater. Interfaces 2015, 7, 6574−6583

(42) Sharma, S.; Srivastava, A. K.; Chawla, S. Self Assembled Surface Adjoined Mesoscopic Spheres of SnO_2 Quantum Dots and Their Optical Properties. *Appl. Surf. Sci.* **2012**, *258*, 8662−8666.
(43) Jood, P.; Mehta, R. J.; Zhang, Y. L.; Peleckis, G.; Wang, X. L.; Siegel, R. W.; Borca-Tasciuc, T.; Dou, S. X.; Ramanath, G. Al-Doped Zinc Oxide Nanocomposites with Enhanced Thermoelectric Properties. *Nano Lett.* **2011**, *11*, 4337−4342.
(44) Lee, K. T.; Lin, C. H.; Lu, S. Y. SnO_2 Quantum Dots Synthesized with a Carrier Solvent Assisted Interfacial Reaction for Band-Structure Engineering of TiO_2 Photocatalysts. *J. Phys. Chem. C* **2014**, *118*, 14457−14463.
(45) Fortunato, E.; Raniero, L.; Silva, L.; Gonc-alves, A.; Pimentel, A.; Barquinha, P.; Aguas, H.; Pereira, L.; Gonc-alves, G.; Ferreira, I.; Elangovan, E.; Martins, R. Highly Stable Transparent and Conducting Gallium-Doped Zinc Oxide Thin Films, for Photovoltaic Applications. *Sol. Energy Mater. Sol. Cells* **2008**, *92*, 1605−1610.
(46) Lee, K. M.; Shih, K. L.; Chiang, C. H.; Suryanarayananc, V.; Wua, C. G. Fabrication of High Transmittance and Low Sheet Resistance Dual Ion Doped Tin Oxide Films and Their Application in Dye-Sensitized Solar Cells. *Thin Solid Films* **2014**, *570*, 7−15.
(47) Kawashima, T.; Matsui, H.; Tanabe, N. New Transparent Conductive Films: FTO Coated ITO. *Thin Solid Films* **2003**, *445*, 241−244.
(48) An, H. R.; Kim, C. Y.; Oh, S. T.; Ahn, H. J. Effect of Sol-Layers on Sb-Doped SnO_2 Thin Films as Solution-Based Transparent Conductive Oxides. *Ceram. Int.* **2014**, *40*, 385−391.

DOI: 10.1021/am508711p
ACS Appl. Mater. Interfaces 2015, 7, 6574−6583